Oscillating Dense Plumes

PAUL R. HOLLAND

British Antarctic Survey, Cambridge, United Kingdom

(Manuscript received 7 July 2010, in final form 23 March 2011)

ABSTRACT

The flow of dense polar shelf waters down continental slopes is a critical component of the global ocean circulation. Recent observations suggest that such plumes can be heavily impacted by tidal variability, and many of the world's important dense-water sources are located in tidally active areas. Tides affect the source of dense water (by modulating the location of hydrographic gradients) and control the subsequent plume mixing and flow path. In an effort to separate these effects, dense plumes are modeled here by extending a classical one-dimensional plume model to two unsteady scenarios in which the plume path is fixed. The first case features a pulsed release of dense water into a stagnant ambient, and the model predicts that gravity waves propagate down the plume. Advective waves in plume density travel with the mean velocity of the current $\overline{U}$ and thus have a wavelength of $\overline{U}P$, the product of plume velocity and the oscillation period P. The second case is of a steady-sourced plume flowing through an ambient that has uniformly oscillating flow. This drives fluctuating shear at the plume–ambient interface (and/or seabed) that leads to variable entrainment of ambient fluid into the plume. Perturbed properties are subsequently advected by the plume, leading to standing "entrainment waves" that also have a wavelength of $\overline{U}P$. Pulsed-source effects may be distinguished from variable-entrainment effects by the phase difference between waves in the different state variables of each plume. Both effects are maximized when the ratio $\overline{U}P/L \approx 1$, where L is the plume length. This condition is satisfied in the Ross Sea, Antarctica, where observations show dense plumes that are strongly affected by tides. Modeled pulsed-source effects qualitatively agree with the observations, implying that hydrographic variability in Ross Sea plumes is associated with variability in their dense-water source rather than unsteady plume mixing. These results might help inform the gathering and interpretation of oceanographic data in tidally active dense-water source regions.

1. Introduction

Sea ice growth over polar continental shelves leads to the formation of cold and saline dense waters that cascade down continental slopes to form the bottom waters that underlie the global oceans (Baines and Condie 1998; Ivanov et al. 2004). This buoyancy-driven flow has many analogs in nature, and its fundamental dynamics have been studied for decades using simple laboratory and mathematical models (e.g., Ellison and Turner 1959, hereafter ET59; Smith 1975). However, recent observations and models of the Ross Sea, Antarctica, have revealed the important effect of tides upon the phenomenon (Whitworth and Orsi 2006; Muench et al. 2009; Padman et al. 2009, hereafter P09; Wang et al. 2010), and under such conditions some tenets of the theoretical understanding break down. Tidal currents in the Ross Sea are unusually strong, but tides are active in all areas of cascading off the Arctic and Antarctic continental shelves (Ivanov et al. 2004; Padman and Erofeeva 2004; P09) and overflowing over the Greenland–Scotland Ridge (Hansen and Østerhus 2000; Padman and Erofeeva 2004). These currents deliver most of the lower limb of the meridional overturning circulation, so their modulation by tides could be globally important.

Localized formation of dense waters on the Ross Sea continental shelf generates the Antarctic Slope Front at the shelf break, which divides dense shelf waters from the lighter deep waters offshore (Jacobs 1991). Strong tides occur along a wide band of the shelf break and slope, and the dominant diurnal harmonics alternately oppose and enhance each other to create a strong fortnightly spring–neap cycle (Erofeeva et al. 2005; P09). During neap tides, the dense shelf waters cascade down the continental slope in relatively steady plumes (Gordon

Corresponding author address: Paul R. Holland, British Antarctic Survey, High Cross, Madingley Road, Cambridge CB3 0ET, United Kingdom.
E-mail: p.holland@bas.ac.uk

DOI: 10.1175/2011JPO4532.1

et al. 2004; Whitworth and Orsi 2006; Gordon et al. 2009; Muench et al. 2009; P09; Wang et al. 2010).

During spring tides, the plume path is altered considerably by the tidal excursion. Spring tidal currents of up to 1 m s^{-1} are so extreme that the slope front can be carried 20 km back and forth across the shelf break every tidal cycle, providing a pulsing source of dense shelf water that dominates the hydrographic variability on the slope (Whitworth and Orsi 2006; P09; Wang et al. 2010). The unsteady tidal current also generates variable amounts of vertical mixing, which controls the overall plume flux by determining the thickness of the benthic layer (Muench et al. 2009; P09; Wang et al. 2010). In a detailed investigation of mixing processes, Muench et al. (2009) found that benthic stress was more important than is usual for plumes, so shear at both the seabed and at the interface between the plume and ''ambient'' water could drive entrainment of water into the plume. Wang et al. (2010) suggest that stronger tides increase the volume of dense water crossing the shelf break but also increase the plume mixing on the slope, so intermediate tides generate the greatest production of dense Antarctic Bottom Water.

The effect of tides on dense plumes might therefore be divided into three broad categories. First, the tide affects the plume path, redirecting the buoyancy-controlled flow of dense water. Where significant fronts exist, tidal excursion can also produce a ''pulsed source'' of dense water that may dominate the subsequent dynamics of the descending flow. Finally, a steady-sourced plume can experience ''variable mixing'' due to oscillating tidal shear at the interface and/or seabed. In this study, the plume path is fixed and the pulsed-source and variable-mixing cases are investigated separately in an effort to distinguish their effects.

Because of their geophysical ubiquity, wall-trapped dense currents have been the subject of a long history of fundamental research. ET59 investigated the situation experimentally and formulated a steady one-dimensional plume model by exploiting the downstream similarity of the flow. Smith (1975) was the first of many to apply this concept to the oceans, extending the theory to the case of a steady ''stream tube'' in a rotating frame. Baines (2005) found experimentally that under certain conditions (primarily shallow bottom slopes) dense flows in a stratified fluid form detraining ''gravity currents'' rather than the entraining plumes studied here. The plume case always occurs in a homogeneous ambient and also appears in many stratified cases, including the Ross Sea (Baines 2008).

Some authors have considered the effect of steady ambient flow on nonrotating plumes (e.g., ET59; Simpson and Britter 1980; Hogg et al. 2005), but it seems that neither the unsteady pulsed-source scenario nor the variable-mixing scenario has been studied in this way before. Pulsed jets, with an intermittent momentum source, have wide application in engineering and biology and have been intensively studied (e.g., see Choutapalli et al. 2009, and references therein), but the closest analog for a buoyancy source concerns the effects of a single change in source strength (Scase et al. 2006, 2009) rather than continual modulation. Baba et al. (2000, 2001) considered the effect of an oscillating water column on the flow of a gravity current but restricted their attention to the advance of its head, rather than the properties of a plume body developed from a continuous source. Models of the oceanic bottom boundary layer consider the general unsteady flow of dense layers (e.g., Killworth and Edwards 1999), but these have not been investigated in the case of an oscillating fluid. P09 and Wang et al. (2010) present full three-dimensional models of tidal dense-water flow in the Ross Sea, but it is hard to isolate the different tidal effects in their comprehensive models.

To the best of the author's knowledge, no simple studies consider the unsteady behavior of dense plumes generated by a pulsed buoyancy source or impacted by oscillatory mixing. These situations are studied in this paper using an unsteady version of the ET59 model. New results arise from the advection of oscillatory properties by a perpetual downslope flow.

2. Model

The motivation of this study is to simplify the pulsed-source and variable-mixing scenarios in order to isolate their underlying features. This requires significant assumptions to reduce the dynamics to their most fundamental form. The most important assumption is the neglect of all flow and gradients in the along-slope direction, which in the oceanographic case amounts to ignoring Coriolis force. The importance of Coriolis force on the scales of the flows studied here is immediately obvious from the observations and any analysis of time or length scales; we examine the nonrotating system only as an analog of the rotating system that is easier to simplify and solve. Restricting our attention to one horizontal dimension allows us to reduce the tides into a unidirectional single harmonic oscillation, removes the complicating effect of plume path advection by the tide, and simplifies the dynamics of the plume to clarify the effects of the different oscillations imposed. The solutions should retain some validity in the rotating case, albeit with the effects propagating within the rotating plume's unsteady across-slope path rather than directly downslope. The nonrotating case is also valid where

plumes are channeled downslope by topography. Care is taken to consider only conclusions that should be independent of this stringent assumption.

The behavior of the complex plume head is also ignored, because it is difficult to model simply, and this restricts our attention to cases in which the oscillation perturbs a continual flow rather than arresting or reversing it. Ross Sea tides are so extreme that this limits our attention to only part of the spring–neap cycle there, but elsewhere this assumption should not be too restrictive. The ambient ocean surrounding the plume is not modeled; to elucidate the basic effects of oscillation in the simplest way possible, it has steady uniform density and is either stagnant or has spatially uniform steady or oscillating flow. The homogeneity of the ambient fluid precludes a study of gravity currents and restricts our attention to the plume regime alone.

The model used to perform both pulsed-source and variable-mixing simulations is an unsteady version of that of ET59 with a few modifications and a change of notation. We consider only time scales much longer than those of the individual eddies and waves affecting the plume–ambient interface, which are a few minutes for the largest, slowest eddies. The dense plumes evolve from specified source conditions in an ambient with specified properties and flow. When required, the tide enters plume dynamics through a body forcing term and the entrainment of ambient momentum into the plume, both of which can be represented as a function of a specified ambient flow velocity. The final system of an active plume flowing beneath a specified ambient is derived from an initial system of an unsteady, two-dimensional, two-layer ocean with free surface, for which it is assumed that the equations are self-explanatory. Quantities used in the final and initial systems are shown in black and gray, respectively, in Fig. 1. Much of the derivation is standard, but it is recounted here to clarify the pressure forcing on the plume in light of the ambient flow. Conservation equations for depth-averaged plume mass, momentum, and buoyancy flux are obtained as follows.

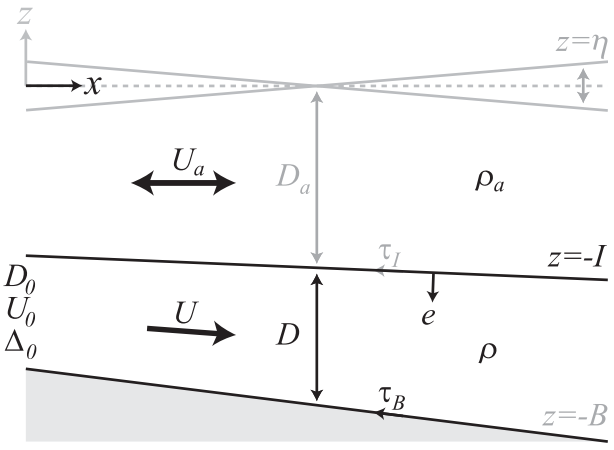

FIG. 1. Schematic of the unsteady plume model, forced by an oscillating ambient and/or variable initial conditions. All quantities are defined in the text. Those shown in gray are used only for model derivation, whereas quantities shown in black appear in the final model used in this paper.

a. Mass

Integrating incompressible mass conservation equations vertically over the unsteady layers shown in Fig. 1, we obtain

$$\frac{\partial D_a}{\partial t} + \frac{\partial (D_a U_a)}{\partial x} = -e \quad \text{and} \tag{1}$$

$$\frac{\partial D}{\partial t} + \frac{\partial (DU)}{\partial x} = e, \tag{2}$$

where $D_a = \eta + I$ is the ambient layer thickness; $D = B - I$ is the plume thickness; η, I, and B are elevations of the free surface, density interface, and seabed, respectively; and e is the rate of entrainment of upper-layer (ambient) fluid into the lower layer (plume). Ambient and plume layer velocities U_a and U are defined by

$$D_a U_a = \int_{-I}^{\eta} u \, dz, \quad DU = \int_{-B}^{-I} u \, dz. \tag{3}$$

b. Momentum

Similarly, integrating equations for the Boussinesq, hydrostatic, and turbulent conservation of momentum, we arrive at

$$\frac{\partial (D_a U_a)}{\partial t} + \frac{\partial (D_a U_a^2)}{\partial x} = -\frac{1}{\rho_0} \int_{-I}^{\eta} \frac{\partial p}{\partial x} \, dz - e U_a - \tau_I \quad \text{and} \tag{4}$$

$$\frac{\partial (DU)}{\partial t} + \frac{\partial (DU^2)}{\partial x} = -\frac{1}{\rho_0} \int_{-B}^{-I} \frac{\partial p}{\partial x} \, dz + e U_a + \tau_I - \tau_B, \tag{5}$$

where ρ_0 is a reference density and τ_I and τ_B are stresses at the interface and seabed, respectively. Drag at the sea surface is neglected, and horizontal turbulent stresses are ignored in consequence of the shallowness of the layers. Entrainment terms are kept explicit because U_a is unsteady. Here, we have used

$$D_a U_a^2 = \int_{-I}^{\eta} u^2\, dz, \quad DU^2 = \int_{-B}^{-I} u^2\, dz, \tag{6}$$

which is strictly correct only if the velocities are piecewise constant. It would be possible to incorporate general velocity profiles into this theory using shape functions (Hogg and Pritchard 2004), but this approach is avoided here for simplicity.

With zero pressure at the sea surface, hydrostatic pressure within the two-layer system is given by

$$p = \begin{cases} \rho_a g(\eta - z) & -I \le z \le \eta \\ \rho_a g(\eta + I) - \rho g(z + I) & -B \le z < -I \end{cases}, \tag{7}$$

where ρ_a and ρ are densities of the upper and lower layers, respectively, and g is the acceleration due to gravity. This allows us to derive the depth-integrated pressure forcing terms,

$$\int_{-I}^{\eta} \frac{\partial p}{\partial x}\, dz = g\rho_a D_a \frac{\partial \eta}{\partial x} \quad \text{and} \tag{8}$$

$$\int_{-B}^{-I} \frac{\partial p}{\partial x}\, dz = g\rho_a D \frac{\partial \eta}{\partial x} - g'\rho_0 D \frac{\partial I}{\partial x} + \frac{gD^2}{2}\frac{\partial \rho}{\partial x}, \tag{9}$$

where $g' = (\rho - \rho_a)g/\rho_0$ is the reduced gravity and we have used the fact that $\partial\rho_a/\partial x = 0$. For simplicity, the smaller final term in (9) will henceforth be neglected (see Killworth and Edwards 1999).

To incorporate both tidal body forcing and the entrainment of ambient momentum into the plume requires that U_a and $\partial\eta/\partial x$ be consistent. We may reasonably assume that the leading-order momentum balance in the upper layer is between the unsteady term and the sea surface slope so that (4) reduces to

$$\frac{\partial (D_a U_a)}{\partial t} = -\frac{g\rho_a D_a}{\rho_0}\frac{\partial \eta}{\partial x}. \tag{10}$$

Fluctuations in the upper-layer flow are the same order as the flow, because the tide reverses, but fluctuations in its thickness (which equal plume-thickness variations by continuity) are typically an order of magnitude smaller than the thickness. For example, Muench et al. (2009) and P09 show plume-thickness variations of 50 and 75 m beneath overlying-fluid thicknesses of 400 and 700 m, respectively. Therefore,

$$\left| D_a \frac{\partial U_a}{\partial t} \right| \gg \left| U_a \frac{\partial D_a}{\partial t} \right|,$$

and we may approximate (10) by

$$\frac{\partial U_a}{\partial t} = -\frac{g\rho_a}{\rho_0}\frac{\partial \eta}{\partial x}. \tag{11}$$

Using (11), assuming that the interfacial stress is encapsulated in the entrainment of momentum, and using a quadratic drag law for the seabed stress, (5) and (9) become

$$\frac{\partial (DU)}{\partial t} + \frac{\partial (DU^2)}{\partial x} = g' D \frac{\partial I}{\partial x} + D\frac{\partial U_a}{\partial t} + eU_a - cU^2, \tag{12}$$

where c is a drag coefficient. To summarize, the terms on the right-hand side of the momentum equation (12) are buoyancy, sea surface slope body force, entrainment of ambient momentum, and seabed drag.

c. Buoyancy

Integrating conservation equations for a scalar quantity ϕ over the shallow layers, we find

$$\frac{\partial (D_a \Phi_a)}{\partial t} + \frac{\partial (D_a U_a \Phi_a)}{\partial x} = -e\Phi_a \quad \text{and} \tag{13}$$

$$\frac{\partial (D\Phi)}{\partial t} + \frac{\partial (DU\Phi)}{\partial x} = e\Phi_a, \tag{14}$$

where turbulent transfer at the interface is again assumed to be encapsulated within entrainment. We have used

$$D_a U_a \Phi_a = \int_{-I}^{\eta} u\phi\, dz, \quad DU\Phi = \int_{-B}^{-I} u\phi\, dz, \tag{15}$$

which implies piecewise-constant scalars in the layers. Using (2), we rewrite (14) as

$$\frac{\partial (D[\Phi - \Phi_a])}{\partial t} + \frac{\partial (DU[\Phi - \Phi_a])}{\partial x} = 0. \tag{16}$$

Assuming that plume density can be reasonably represented as a linear function of scalar quantities such as temperature and salinity, we convert (16) to an expression for the conservation of plume buoyancy flux,

$$\frac{\partial (Dg')}{\partial t} + \frac{\partial (DUg')}{\partial x} = 0. \tag{17}$$

For the remainder of the paper, the reduced gravity g' will be expressed in terms of the plume–ambient density anomaly $\Delta = \rho - \rho_a$, which is hereafter referred to as density to avoid confusion later on.

d. Entrainment

In plume flow, the entrainment of ambient fluid is the sole effect of vertical mixing, so the entrainment parameterization is central to the results of variable-mixing simulations. Entrainment into oceanic plumes is well summarized by Cenedese and Adduce (2010) and references therein. There are three main sources of mixing that drive entrainment: hydraulic jumps, shear at the plume–ambient interface, and shear or roughness effects in the bottom boundary layer. Mixing in hydraulic jumps is vigorous but localized and is not considered here. Interfacial instability is usually held to be dominant in ocean plumes, but superimposing a barotropic tidal forcing on the plume increases the importance of boundary-driven mixing (Muench et al. 2009), so it is unclear whether standard formulations based solely upon interfacial mixing are valid. For clarity, entrainment is parameterized in this study as a simple linear function of interfacial shear, and other more detailed formulations are later employed in a sensitivity study. The case of detrainment into a stratified ambient (Baines 2005) is not considered.

The simplest way to represent mixing driven by the shear between a moving plume and stationary ambient is by using the similarity entrainment assumption,

$$e_{\mathrm{sm}} = E|U|\,, \tag{18}$$

which becomes a shear assumption,

$$e_{\mathrm{sh}} = E|U - U_a|\,, \tag{19}$$

in the case of a nonstationary ambient (ET59). For simplicity, the default entrainment formulation in this study is (19), with E set to a constant value. This linear relation between mixing and shear clarifies the effects of oscillation because it leaves the time-mean properties of the plume unaffected; in a uniformly oscillating flow, positive entrainment perturbations are offset by subsequent negative perturbations so that the mean over an oscillation cycle is zero. However, using a constant value for E is clearly unphysical, so we also perform sensitivity studies with more complex entrainment parameterizations. It is unclear if boundary mixing or interfacial shear is more important in tidal cases (Muench et al. 2009), so one parameterization of each is tested.

A widely used parameterization of entrainment driven by interfacial shear but also suppressed by stratification is given by Turner (1986). The formula allows mixing up to a critical value of the bulk Richardson number,

$$e_{\mathrm{Ri}} = \begin{cases} \dfrac{0.08 - 0.1\mathrm{Ri}}{1 + 5\mathrm{Ri}}|U - U_a| & 0 \le \mathrm{Ri} \le 0.8 \\ 0 & \mathrm{Ri} > 0.8 \end{cases}, \tag{20}$$

where

$$\mathrm{Ri} = \frac{g'D}{|U - U_a|^2}\,. \tag{21}$$

Parameterizations of plume entrainment driven by boundary mixing are far rarer, so a formula is adapted from that of Legg et al. (2006). Extraction of energy from the mean flow by turbulence leads to a mean mixing energy production of

$$P_b = \frac{cU^3}{D}\,. \tag{22}$$

If we assume that this energy is dissipated within the plume, driving diapycnal mixing with an efficiency $\gamma = 0.2$, the associated vertical diffusivity (Osborn 1980) is

$$K = \frac{\gamma P_b}{N^2}\,. \tag{23}$$

Substituting for the buoyancy frequency $N^2 = g'/D$ and converting this diffusivity to an entrainment rate using $e_{\mathrm{Lg}} = K/D$, we obtain

$$e_{\mathrm{Lg}} = \frac{\gamma c U^3}{g'D}\,. \tag{24}$$

e. Forcings

Pulsed-source and variable-mixing simulations are performed by solving the governing equations under a range of different forcings, as detailed in Table 1. In each simulation, one forcing is varied while the others are held steady at their mean value. In each pulsed-source simulation, the plume source thickness or density is varied about a given mean according to a simple sinusoid with period P and a given half amplitude,

$$D_0 = \overline{D}_0 + \hat{D}_0 \sin\left(\frac{2\pi t}{P}\right) \quad \text{and} \tag{25}$$

$$\Delta_0 = \overline{\Delta}_0 + \hat{\Delta}_0 \sin\left(\frac{2\pi t}{P}\right). \tag{26}$$

Variable-mixing simulations are undertaken by sinusoidally varying a spatially uniform ambient velocity,

$$U_a = \overline{U_a} + \hat{U}_a \sin\left(\frac{2\pi t}{P}\right). \tag{27}$$

The use of a uniform ambient flow neglects any spatial variation in tidal flow with seabed depth (e.g.,

TABLE 1. Description of the model setup for each simulation referred to in the text. The mean value and, where applicable, period and half amplitude of any oscillation are given for each of the forcings (source plume thickness D_0, source density anomaly Δ_0, and ambient velocity U_a). The choice of formulation for the entrainment and momentum source boundary condition is also stated.

Identifier	P (h)	$\overline{D}_0$ (m)	$\hat{D}_0$ (m)	$\overline{\Delta}_0$ (kg m^{-3})	$\hat{\Delta}_0$ (kg m^{-3})	$\overline{U_a}$ (m s^{-1})	$\hat{U}_a$ (m s^{-1})	Entrainment	Momentum
					Base case				
B	—	100	0	0.2	0	0	0	e_{sh}	Quadratic
					Pulsed source				
D1	—	50	0	0.2	0	0	0	e_{sh}	Quadratic
D2	—	150	0	0.2	0	0	0	e_{sh}	Quadratic
D3	24	100	50	0.2	0	0	0	e_{sh}	Quadratic
D4	12	100	50	0.2	0	0	0	e_{sh}	Quadratic
D5	48	100	50	0.2	0	0	0	e_{sh}	Quadratic
G1	—	100	0	0.15	0	0	0	e_{sh}	Quadratic
G2	—	100	0	0.25	0	0	0	e_{sh}	Quadratic
G3	24	100	0	0.2	0.05	0	0	e_{sh}	Quadratic
					Variable mixing				
U1	—	100	0	0.2	0	+0.25	0	e_{sh}	Cubic
U2	—	100	0	0.2	0	−0.25	0	e_{sh}	Cubic
U3	24	100	0	0.2	0	0	0.25	e_{sh}	Unsteady
U4	24	100	0	0.2	0	0	0.5	e_{sh}	Unsteady
U5	24	100	0	0.2	0	0	0.75	e_{sh}	Unsteady
U6	12	100	0	0.2	0	0	0.5	e_{sh}	Unsteady
U7	48	100	0	0.2	0	0	0.5	e_{sh}	Unsteady
E1	24	100	0	0.2	0	0	0.5	0	Unsteady
E2	24	100	0	0.2	0	0	0.5	$e_{sh}/2$	Unsteady
E3	24	100	0	0.2	0	0	0.5	e_{sm}	Unsteady
E4	24	100	0	0.2	0	0	0.5	e_{Ri}	Unsteady
E5	24	100	0	0.2	0	0	0.5	e_{Lg}	Unsteady

continuity-preserving acceleration in shallower water) or sea surface slope (e.g., different sections of the tidal height anomaly). The ambient flow is chosen such that it never reverses or exceeds the plume flow, because both contravene the assumptions of a continuous buoyancy-driven plume (ET59). For brevity, this study does not consider in detail the case of an ambient oscillation superimposed on mean ambient flow (using e_{sm} or e_{sh}, the results of such a case could be obtained by superposition of results from the steady-mean-flow and oscillating-ambient cases studied here).

The boundary condition for plume velocity, which is described in the appendix and Table 1, is more complex. ET59 show that plumes rapidly adjust from arbitrary source conditions to a "normal" state in which U, dD/dx, and DUg' are constant (so $U \sim$ constant, $D \sim x$, and $\Delta \sim x^{-1}$). The oscillating forcings used here continually affect both the normal state and its adjustment length scale. We are primarily concerned with variations in the normal state, rather than variable adjustment from arbitrarily chosen boundary conditions, so the source plume velocity is set to be as close as possible to the (potentially oscillating) normal state to remove the adjustment region altogether. This is physically justified because dense-water sources should not resist adjustment any more than their ensuing plume. Previous authors have used a simple force balance to obtain a normal-state source velocity, so in the appendix this approach is extended to the unsteady case.

f. Solution routine and parameter choices

Using an entrainment parameterization and appropriate forcings, Eqs. (2), (12), and (17) are solved numerically on a staggered grid using a two-time-level explicit routine. Advection terms are treated using simple upwinding, and all other terms use central differences. Results demonstrated grid independence with a 1-km grid and 20-s time step. Source properties and ambient flow are set to steady mean values until the plume attains steady state, when the pulsed source or oscillating ambient is introduced and the run continued until the plume attains cyclic equilibrium, of which the final cycle is analyzed.

The values of plume forcings are given in Table 1. The parameters used in this study are inspired by real plumes and serve to illustrate important features of the oscillating behavior. All plumes descend down a slope that drops 1000 m over a distance of 100 km, which is representative of the gradients present in nature (Price and Baringer 1994; Ivanov et al. 2004). Source thicknesses of 100 m (Price and Baringer 1994) and density

anomalies of 0.2 kg m^{-3} (Ivanov et al. 2004) are representative values for dense cascades. In pulsed-source simulations, the source oscillation amplitudes are 100 m and 0.1 kg m^{-3}. In variable-mixing simulations, the ambient flow velocity oscillates about zero with a range of amplitudes of up to 0.75 m s^{-1} (Padman and Erofeeva 2004; P09). Tides are crudely represented by a single harmonic oscillation, usually at a diurnal frequency (P = 24 h). Because this paper focuses solely on the qualitative effects of tidal forcing, $E = 0.002$ is arbitrarily chosen so that the source thickness of 100 m is tripled over the 100-km domain. A standard drag coefficient of $c = 0.003$ is used.

3. Results

The basic settings described above are used in a steady ''base'' simulation (case B; Table 1), which is perturbed in various ways to obtain all other results. For each set of simulations with an oscillating forcing, two steady ''bracketing'' simulations are performed in which the parameter under consideration is set to the extreme values of the oscillation. Pulsed-source simulations have an unsteady source thickness (D3–D5) or density (G3), quadratic normal-state source velocity, and zero ambient flow. Variable-mixing simulations (U3–U7 and E1–E5) have a steady source, oscillating ambient flow, and an unsteady normal-state source velocity. A basic description of the model results is given here, with discussion presented in the next two sections.

a. Steady ambient, pulsed-source thickness

Figure 2 (left) shows the envelope of curves described by hourly snapshots of the three state variables throughout a 24-h equilibrium cycle of the pulsed-source-thickness case D3. Snapshots at selected times are highlighted in color, and Fig. 2 (right) shows these results as anomalies from the base case. Also plotted in black in Fig. 2 (right) is the mean profile in the oscillating case. Results plotted in dark blue are from the base and bracketing cases, which use mean and extreme source thicknesses, respectively. The normal states discussed in section 2e are visible in these steady cases; plume thickness increases uniformly with distance due to entrainment, velocity is constant, and density decreases as the reciprocal of distance. The normal state is shifted according to the change in the steady source.

Before we consider the results of oscillating-source scenarios, it is instructive to consider some analytical conclusions from the reduced system of a dense fluid release at $x = 0$ with neglect of ambient flow, entrainment, drag, and seabed slope,

$$\frac{\partial D}{\partial t} + \frac{\partial (DU)}{\partial x} = 0 \quad \text{and} \tag{28}$$

$$\frac{\partial (DU)}{\partial t} + \frac{\partial (DU^2)}{\partial x} - g' D \frac{\partial D}{\partial x} = 0, \tag{29}$$

where g' is now constant because of the lack of entrainment. Whitham (1974) outlines the method by which the solution to this hyperbolic system can be obtained by considering the Riemann invariants $U \pm 2\sqrt{g'D}$ on the characteristic curves $C_{\pm}: dx/dt = U \pm \sqrt{g'D}$. The complete solution for any particular application is governed by the propagation of the boundary and initial conditions along the characteristics. In the present problem, the upstream-propagating waves on C_- characteristics originate in the quiescent water lying ahead of the plume in space and time. Therefore, the solution is dominated by downstream-propagating waves on C_+ characteristics, which originate in the boundary conditions at $x = 0$ and travel at a rate of $U + \sqrt{g'D}$, the inherent plume flow speed plus its gravity wave speed. The characteristics of the full system (2), (12), and (17) remain $C_{\pm}: dx/dt = U \pm \sqrt{g'D}$, plus the particle paths P: $dx/dt = U$. It is not possible to determine the complete solution in this case, however, because the Riemann variables are not invariant along characteristics.

Scase et al. (2006, 2009) show that a single change in source buoyancy flux causes plume properties to switch permanently between the normal states corresponding to the initial and perturbed sources. In case D3, continual oscillation in the plume source leads to waves that travel along the plume, oscillating about a mean that closely follows the normal state of the base case by construction of the simple linear entrainment e_{sh} (see section 2d). The wave amplitudes are limited near the source by the normal states of the bracketing cases and subsequently decay from this limit. The varying source thickness is carried downstream by plume flow, leading to ''advective'' waves in that quantity. However, these waves in thickness are actually shallow-water gravity waves in the plume–ambient interface. As expected from the above discussion of characteristics, their overall phase speed is therefore similar to the sum of the plume velocity and the shallow-water gravity wave speed. Waves in plume thickness and velocity are locked in phase with each other by inertial, entrainment, and buoyancy terms in the governing equations.

Steady plumes with a larger source thickness maintain a higher density, because at a given distance from the source a higher proportion of the plume is source water rather than entrained ambient. In the case of an oscillating source thickness, pulses of higher density are initiated whenever the source thickens. However, unlike

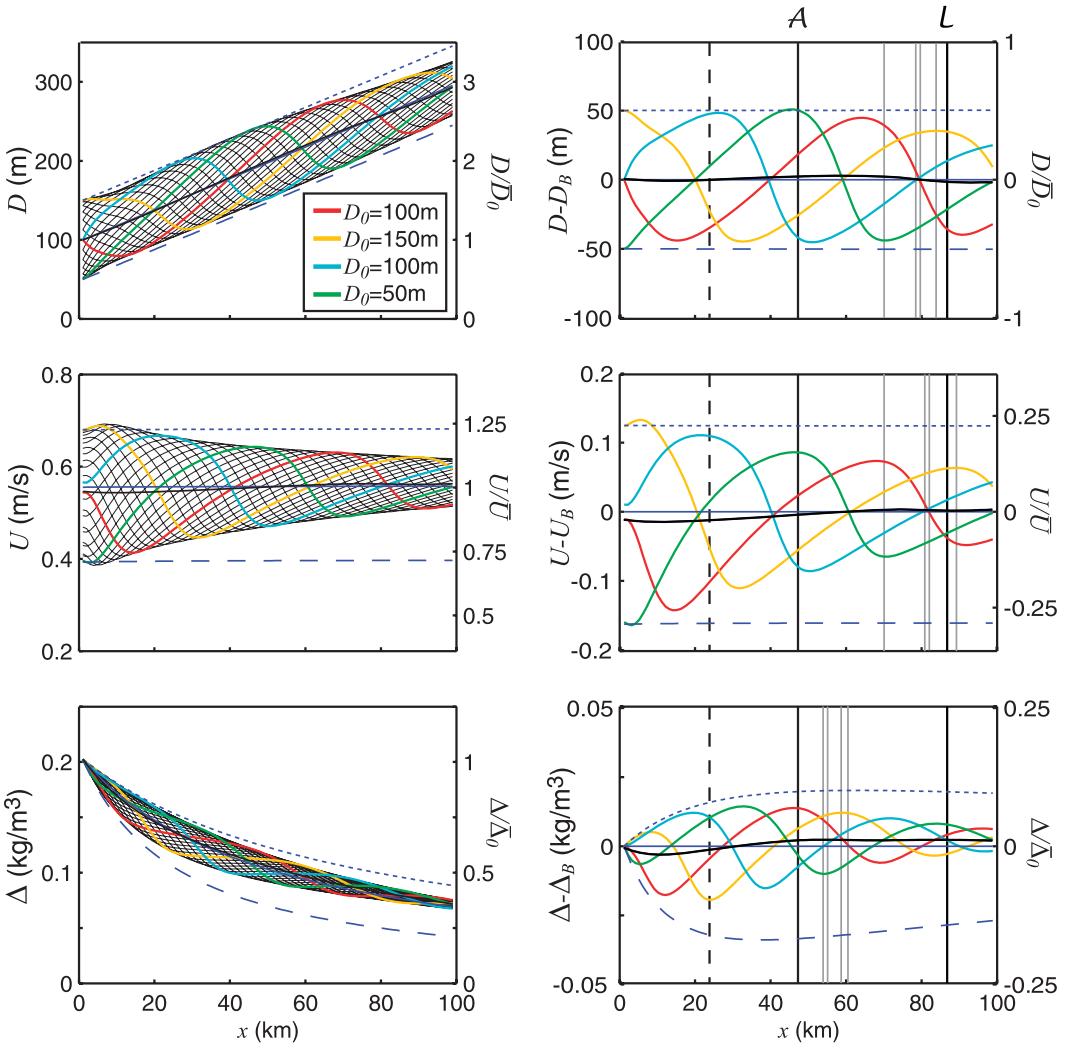

FIG. 2. Results from the cyclic equilibrium state of run D3, in which the source thickness oscillates. (left) The results throughout the equilibrium state, with results plotted in black every hour for the final cycle of the run ($P = 24$ h). Also plotted in dark blue are the steady runs B (solid; $D_0 = 100$ m), D1 (dashed; $D_0 = 50$ m), and D2 (dotted; $D_0 = 150$ m). Selected snapshots of the results from different stages of the cyclic forcing are plotted in color. The oscillating source initiates waves that travel down the plume, with an amplitude bounded by the steady bracketing cases. (right) The waves are emphasized by plotting the results as an anomaly from those of the steady base case B; mean results over the cycle are indicated by a black line. Black vertical lines show the value of characteristic scales described in the text, and gray lines illustrate the size of the first wavelength at each of the snapshot times. Waves in plume thickness and speed are advected gravity waves, with wavelength $\mathcal{L}$, whereas waves in plume density anomaly are purely advective, with length scale $\mathcal{A}$. The vertical dashed line indicates the position $\mathcal{A}/2$ at which the time series in Fig. 3 is shown.

the waves in thickness and velocity, these density pulses travel at a rate closer to the advective speed and do not follow the gravity wave propagation. Gravity waves can only affect plume density indirectly, by altering the entrainment via the plume velocity. An alternative view of this situation is that after simple manipulation the buoyancy flux equation (17) is already in characteristic form, with characteristic velocity U of the particle paths rather than traveling waves (Whitham 1974). The advective waves in density are eventually dissipated because the faster phase speed of waves in thickness and velocity prevents a coherent anomaly in the three state variables from persisting. This relaxation of the plume density toward the base case in turn dissipates the waves in buoyancy forcing and hence plume velocity.

To demonstrate these arguments, we define length scales determined by the distance traveled by parcels moving at the plume velocity and shallow-water gravity wave speed for the plume over a tidal period. The simplest advective length scale is

$$\mathcal{A} = \overline{U}P, \tag{30}$$

where velocity is averaged temporally over a tidal period and spatially over the entire domain. The simplest total length scale for advection plus gravity wave propagation is

$$\mathcal{L} = \overline{(U + \sqrt{g'D})}P. \tag{31}$$

Both of these quantities are plotted in Fig. 2 (black vertical lines), and for comparison the plume's first wavelength has also been highlighted at different stages of the forcing cycle (gray vertical lines). Waves in thickness and velocity have a wavelength similar to $\mathcal{L}$, that of advected gravity waves, whereas waves in density have a wavelength closer to $\mathcal{A}$, from pure advection. This conclusion is confirmed by a sensitivity study in which the reduced gravity and bedrock slope are independently varied (not shown); both plume velocity and gravity wave speed respond to the reduced gravity, but the plume velocity alone responds to the bedrock slope.

Modeled wavelengths vary during the forcing cycle because varying the source thickness affects plume flow and gravity wave propagation. Over the first wave (distances less than one wavelength from the source) the perturbations are particularly large relative to the variables' mean values, and the resulting velocity variations cause variable wavelengths and wave asymmetry. Using the methods of Whitham (1974) and Lighthill (1978) to assess the system (28) and (29) forced by the boundary condition (25) shows that, in this simplified case, the waves initiated by the oscillating source should break after traveling about 50 km. However, the lack of evidence of wave breaking in the full system (Fig. 2) implies that this effect is suppressed, perhaps by the effects of nonlinear seabed drag, entrainment, or numerical diffusion.

These results can also be viewed as a time series of model results at a fixed point. The series in Fig. 3 is taken at the location of $\mathcal{A}/2$ (as shown in Fig. 2). All waves have a period of P and, by virtue of the location, a phase difference of approximately $P/4$ from the oscillating boundary condition (Fig. 2). The time series shows the tight coupling between asymmetric waves in plume thickness and velocity. Waves in plume thickness and velocity are slightly out of phase with those in density, in keeping with their different phase speed. The wave in entrainment follows the fluctuation in flow velocity.

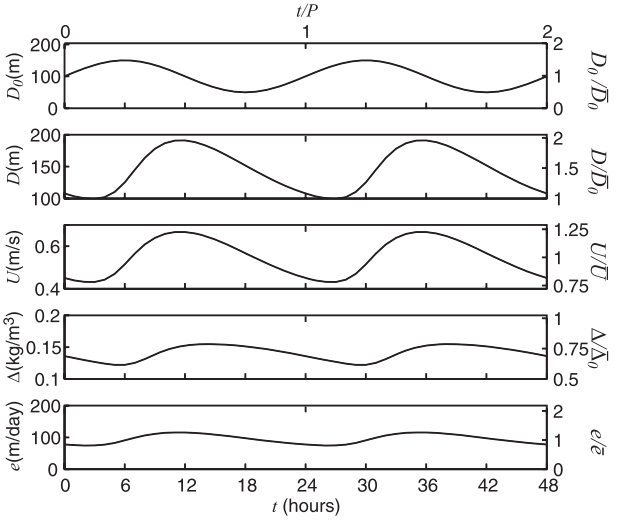

FIG. 3. Two cycles from the equilibrium state of run D3, in which the source thickness oscillates. (top) The source thickness and (top middle)–(bottom) plume results from the location $\mathcal{A}/2$, as indicated in Fig. 2. The advected gravity waves in plume speed and thickness lag the forcing by approximately $P/4$ by virtue of the position of the time series, and the slower advective wave in plume density anomaly has a greater lag.

b. Steady ambient, pulsed-source density

Results from case G3, which has an oscillating source density, adhere to similar principles (Fig. 4). The oscillating source causes waves in the plume density with the advective wavelength and an amplitude bounded by the bracketing steady cases. The ensuing alterations to the plume buoyancy excite waves in plume velocity that travel at a rate closer to the advective plus gravity wave speed. The difference in phase speed between waves in plume velocity and density again leads to downstream decay in the amplitude of waves in density.

Steady alterations to the source density have no effect on the thickness profile (Fig. 4), because, in the steady normal state with similar entrainment, U is constant and (2) collapses to $\partial D/\partial x = E$. In case G3, the variable buoyancy forcing causes waves in the plume velocity, the normal state is untenable, and waves in plume thickness result. These waves again have a wavelength similar to those of velocity; the fixed source thickness is presumably responsible for the lack of an exact correspondence between the two.

The G3 time series (Fig. 5) shows that (appropriately for an advective wave) plume density is almost perfectly antiphase with the source density prescribed at a distance of $\mathcal{A}/2$ upstream. Other quantities have different wavelengths and thus phase differences from the forcing. Waves are less asymmetric than those of case D3, because the velocity perturbations are much smaller.

c. Variable mixing, steady source

1) BASIC RESULTS

Figure 6 shows the same quantities for the variable-mixing simulation U4. The effect of steady ambient flow

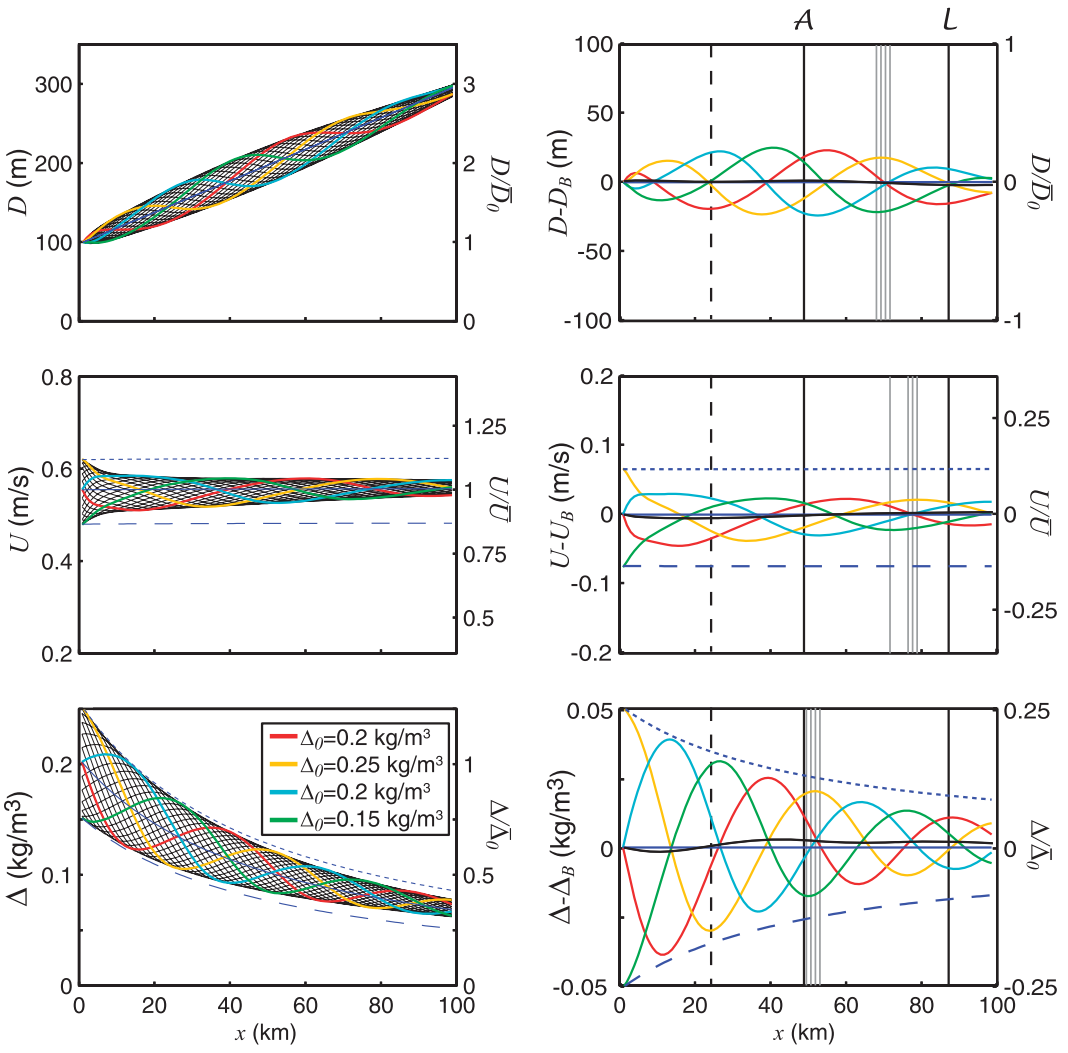

FIG. 4. Results from the cyclic equilibrium state of run G3, in which the source density anomaly oscillates. As in Fig. 2, but the dark blue lines are runs B (solid; $\Delta_0 = 0.2$ kg m^{-3}), G1 (dashed; $\Delta_0 = 0.15$ kg m^{-3}), and G2 (dotted; $\Delta_0 = 0.25$ kg m^{-3}), and the vertical dashed line locates the time series in Fig. 5.

is shown by the normal states of the bracketing cases. An opposing ambient flow increases shear-driven entrainment, which decelerates and thickens the plume and decreases its density (ET59). A coflowing ambient has the opposite effect. However, these bracketing cases are less appropriate in variable-mixing simulations. U1 and U2 necessarily have a lower ambient flow magnitude than the extremities of U4 (Table 1), because a more appropriate bracketing case with $U_a = 0.5$ m s^{-1} would have effectively no shear, no entrainment, and therefore no plume. More significantly, the dominant sea surface slope body force in (12) disappears in steady cases as a result of the assumption (10) that the dominant ambient momentum balance is between the unsteady term and sea surface slope; a balance between advection and sea surface slope would be more appropriate in these cases.

The variable-mixing results are significantly different from those of the pulsed-source cases. Ambient flow affects the whole length of the plume, so the plume velocity contains a cycle that is similar throughout the domain rather than emanating from the source. The direct sea surface slope body forcing is the dominant term in the momentum balance (12) and leads to a plume that oscillates broadly in phase with the ambient and with a similar amplitude of oscillation. To a reasonable level of approximation, the plume flow is simply the ambient oscillation superimposed on a steady downslope flow.

Density clearly contains asymmetric waves at the advective-length scale, but these are standing "entrainment waves" rather than the traveling advective waves observed in the previous simulations. Density variations are caused by entrainment, which here oscillates about

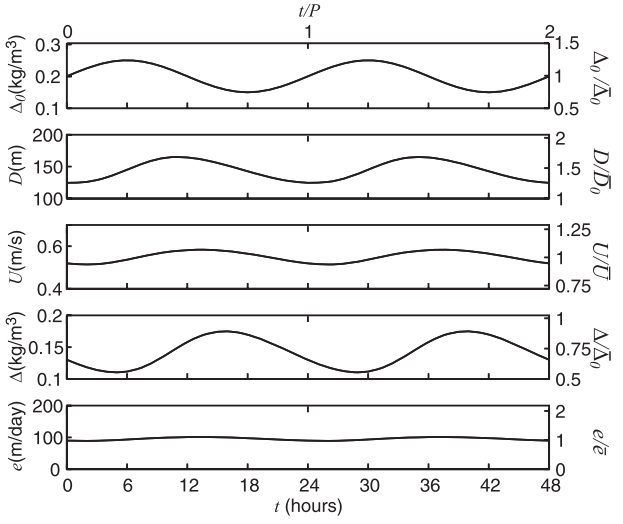

FIG. 5. Two cycles from the equilibrium state of run G3, in which the source density anomaly oscillates. As in Fig. 3, but (top) showing the source density anomaly.

its case-B value in time but is relatively uniform in space. A parcel of fluid following the plume accumulates the time history of entrainment anomalies, creating an advective-length standing wave. Parcels that have traveled a distance of $\mathcal{A}$ or multiples of $\mathcal{A}$ from the source have experienced one or more complete anomaly cycles. Because entrainment is a linear function of shear, positive perturbations to the entrainment are offset by subsequent negative perturbations, and the net perturbation over a whole oscillation cycle (i.e., that experienced by a parcel of fluid that has traveled a distance of $\mathcal{A}$) is zero; the density equals that of the base case there at all times. By the time the parcels have reached $\mathcal{A}/2$ from the source, they have experienced approximately half of an entrainment anomaly cycle, so the density is highest there when entrainment returns to its mean value after a half cycle of negative anomalies (coflowing ambient). The pattern, amplitude, and phase of the entrainment waves are determined by the anomaly that arises from the chosen entrainment parameterization.

In common with the other variables, thickness varies across the whole plume during the tidal cycle rather than admitting traveling gravity waves. Through their link with entrainment, waves in thickness could be expected to be equal to and opposite of those in density. They are of the opposite sign but clearly not mirror images.

The time series in Fig. 7 allows us to further examine the unsteady entrainment that generates the waves shown in Fig. 6. As described above, the strong forcing from the sea surface slope keeps the plume velocity in phase with the ambient velocity to leading order. The entrainment is a linear function of the shear between the two, so this implies a steady entrainment rate. It is only the combined effect of the other forcings in the plume momentum equation (buoyancy, momentum entrainment, and drag) that cause unsteady shear and entrainment, and therefore entrainment waves. The sum of buoyancy and momentum entrainment is a roughly steady acceleration, but the nonlinearity of the seabed drag provides a significant deceleration of the plume (relative to the ambient) when the downslope flow is high. Therefore, the sum of the forcings that cause shear drops below zero whenever peak downslope flow occurs but is positive otherwise. The peak shear-causing acceleration thus occurs at the minimum drag, when the ambient velocity is directed upslope (time A in Fig. 7). The peak shear and hence entrainment anomaly occurs $P/4$ later, when the shear-causing acceleration switches from positive to negative (time B). The lowest plume density occurs when the entrainment anomaly switches from positive to negative (time C). For the remainder of the paper, we will consider only plume density, because it clearly illustrates the entrainment waves and is the easiest quantity to observe in the oceans.

2) EFFECT OF AMBIENT OSCILLATION MAGNITUDE

Figure 8a shows cases U3–U5 (ambient flow oscillations of half amplitude 0.25, 0.5, and 0.75 m s^{-1}, respectively), which could be taken to represent three case studies from the spring–neap cycle. All have standing entrainment waves at the advective length scale. U3 and U4 density profiles both oscillate around the base case, with smaller-amplitude waves in case U3 because the weaker ambient oscillation causes smaller entrainment anomalies.

In case U5, the density oscillations are about a lower mean profile because the entrainment is increased on average. The plume velocity in case B is $\approx$0.55 m s^{-1}, so an oscillating ambient with half amplitude 0.5 m s^{-1} will always be slower, whereas an ambient flowing at up to 0.75 m s^{-1} will overtake the plume. The entrainment $e_{sh} = E|U - U_a|$ is a linearly decreasing function of U_a for $U_a < U$, so entrainment oscillates uniformly about its base-case value as U_a varies and the mean plume density is unaffected. However, e_{sh} is linearly increasing for $U_a > U$, so the symmetry of entrainment anomalies about the base-case mean is broken for part of the cycle and the mean plume entrainment (density) increases (decreases). This illustrates the central importance of the entrainment formulation to the qualitative results of this study. The results of case U5 are included for illustrative purposes only, because plume assumptions are inappropriate when the ambient drags the plume forward (ET59).

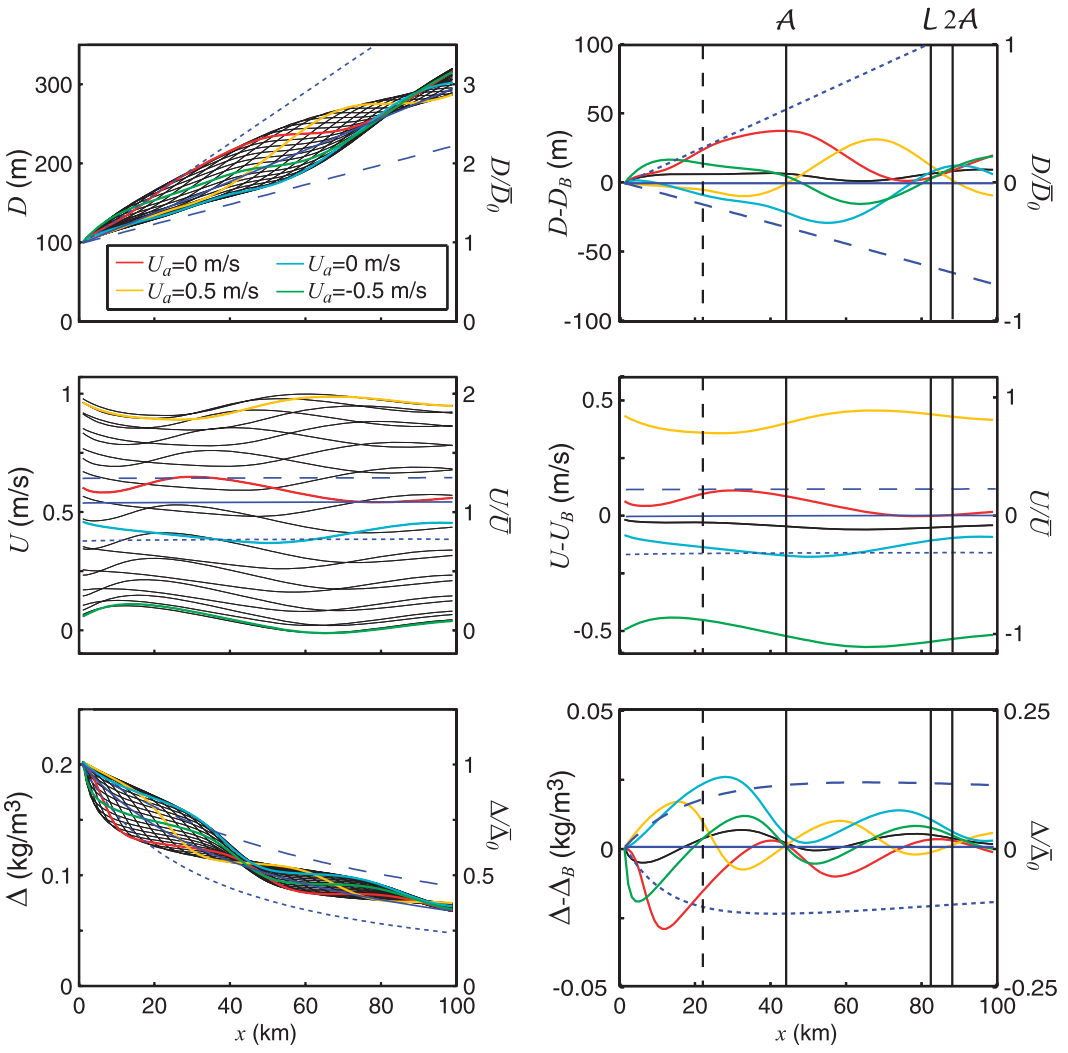

FIG. 6. Results from the cyclic equilibrium state of run U4, in which the ambient flow velocity oscillates. As in Fig. 2, but the dark blue lines are runs B (solid; $U_a = 0$ m s^{-1}), U1 (dashed; $U_a = 0.25$ m s^{-1}), and U2 (dotted; $U_a = -0.25$ m s^{-1}), and the vertical dashed line locates the time series in Fig. 7. The oscillating sea surface pressure forcing causes the plume speed to oscillate. The plume experiences seabed drag and buoyancy forcing, unlike the ambient, so shear between the two causes time-variable mixing that leads to standing entrainment waves in plume density and thickness.

3) EFFECT OF ENTRAINMENT FORMULATION

The most significant assumption to the results of variable-mixing cases is that entrainment is a linear function of shear, so we now investigate different entrainment rates and formulations. Figure 9a shows the results of cases E1, E2, and U4, which have the same shear entrainment, but with coefficients of $E = 0$, 0.001, and 0.002, respectively. Increasing the entrainment thickens the plume on average and also increases the amplitude of the entrainment waves. It also reduces the mean plume speed, because entrainment is proportional to shear; entrainment is highest when the ambient flow opposes the plume, so proportionately more decelerating ambient momentum is entrained.

For illustrative purposes, Fig. 9a also shows a case (E3) in which an oscillating ambient is used with the similarity entrainment assumption (18). The density is identical to the steady normal state of the base case. The normal solution of case B has $\partial U/\partial x = 0$, permitting a nontrivial solution of the steady version of (2) when $\partial D/\partial x = E$, which implies that $\Delta \sim x^{-1}$. The only difference in case E3 is the oscillating ambient acceleration on the right-hand side of (12); unlike case U4, U_a does not appear on the right-hand side of (2). Adding a spatially uniform acceleration oscillates U but does not

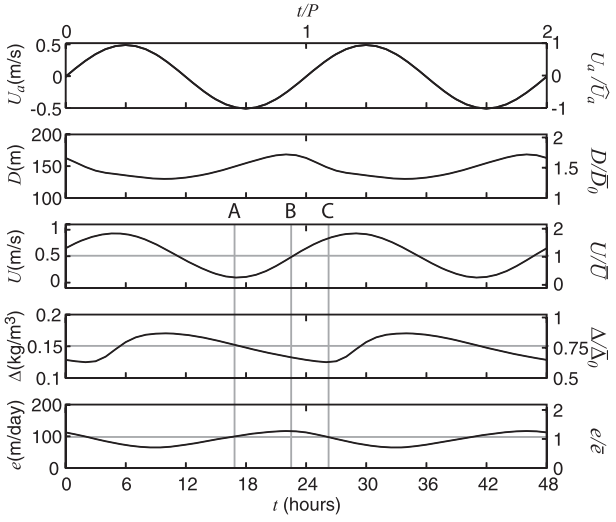

FIG. 7. Two cycles from the equilibrium state of run U4, in which the ambient flow oscillates. As in Fig. 3, but (top) showing the ambient flow speed. The ambient and plume speeds are almost in phase, but small differences lead to shear entrainment and thus standing oscillations in plume thickness and density. Points A, B, and C are discussed in the text.

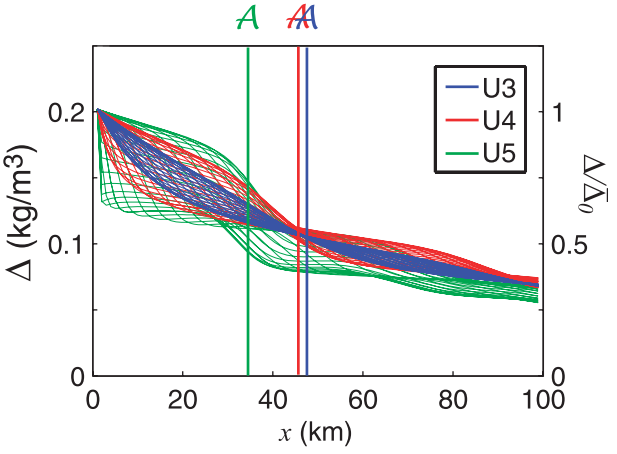

FIG. 8. Density anomaly results from the cyclic equilibria of runs U3–U5, which have oscillating ambient flow of half amplitude $\hat{U}_a = 0.25$, 0.5, and 0.75 m s^{-1}, respectively. Increasing the oscillation increases the amplitude of the standing waves.

preclude $\partial U/\partial x = 0$, so the normal solution with $\partial D/\partial x = E$, $\Delta \sim x^{-1}$ is permitted as before. Though clearly unphysical, this is an important illustrative result; without external perturbation to its mixing, the plume can accommodate a changing flow velocity without change in its other state variables.

Figure 9b shows the effect of varying the entrainment formulation. The commonly used Turner (1986) parameterization (case E4) uses a complex function of shear and stability, but the results again show entrainment waves in plume density that oscillate about the mean profile. The phase of the entrainment waves is identical to that of the case with entrainment parameterized as a linear function of shear (cf. Fig. 6), but the plume properties do not return to base-case values at multiples of $\mathcal{A}$ because the entrainment is no longer symmetric around zero ambient flow. Entrainment is suppressed for high Ri, so for low shear there is no entrainment at all, but entrainment increases sharply for the highest rates of shear when the ambient flow opposes the plume. This results in the steplike boundaries to the envelope of plume results; for low shear the density is advected unchanged, leading to horizontal boundaries, and for high shear there are rapid bursts of entrainment, causing steeply falling boundaries.

The results of case E5, which has entrainment parameterized as a function of boundary-driven mixing, also display entrainment waves. Variations in entrainment from boundary mixing are dominated by its proportionality to the cube of plume velocity, so peak entrainment occurs when the plume flow is strongest. This occurs when the ambient flow is directed downslope, so the result is the exact opposite of that for shear-driven entrainment, which peaks when the ambient flow is upslope. Comparison of the density profiles in Figs. 6 and 9 confirm that their entrainment waves have opposing phases.

4. Discussion

Tides affect dense-water plumes by causing pulsing of their dense-water source, time-variable mixing of the resultant plume, and lateral advection of the plume path. The overall effect is the combination of all three, but in this study we neglect the latter and consider the first two in isolation to evaluate their qualitative behavior. Plume advection turns source pulses into traveling gravity waves and accumulates the density anomaly caused by time-variable mixing into a standing entrainment wave. These along-plume variations would be superimposed upon each other and the unmodeled lateral alteration of the plume path by tides.

Tides will always cause mixing to oscillate, but a pulsed source will only occur if a hydrographic front is repeatedly advected across the shelf break. Local hydrography therefore determines which of the waves is most important. The amplitude of traveling waves is determined by the size of the pulse at the source, which would be related to the amplitude of the tide and strength of the lateral gradient at the front. Results indicate that decay of the traveling waves in plume thickness is small but that shorter waves in density are rapidly damped.

In variable-mixing cases, standing entrainment waves are caused by oscillating mixing acting upon a layer with

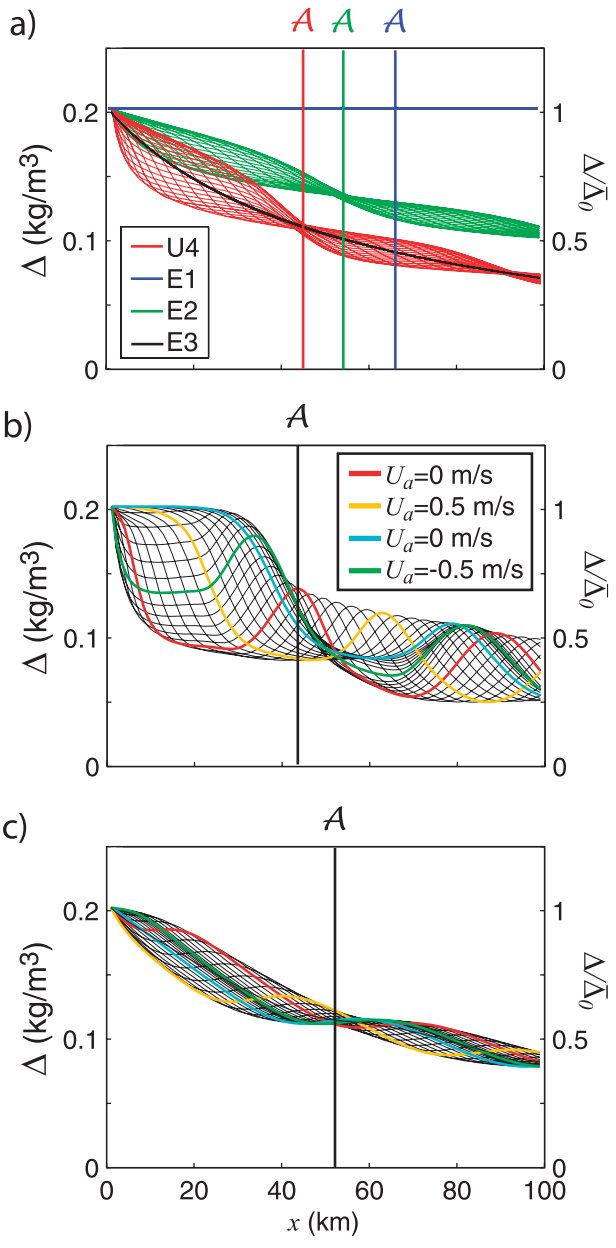

FIG. 9. Density anomaly results from the cyclic equilibria of runs (a) E1, E2, U4, and E3, which have shear-based entrainment with coefficient $E = 0$, 0.001, and 0.002 and similarity entrainment, respectively, and (b) E4 and (c) E5, which have different entrainment parameterizations. Increasing entrainment decreases the mean density anomaly between plume and ambient and increases the amplitude of the standing waves. Modified standing waves occur in simulations with more realistic entrainment parameterizations.

mean flow; to the knowledge of the author, this type of entrainment wave does not appear elsewhere in the literature. The importance of these waves is critically dependent upon the entrainment assumption, with their amplitude being governed by the unsteady deviation of entrainment from its mean value. The phase of entrainment waves relative to that of the forcing depends upon the assumption used, with opposing effects caused by boundary- and interfacial-led instability. Given an entrainment parameterization, the amplitude of entrainment waves is determined by the amplitude of the oscillating forcing.

Pulsed-source and variable-mixing waves have different relative characteristics between the different plume variables. In the pulsed-source-thickness case, tightly coupled traveling waves in plume thickness and velocity (hence entrainment) have a phase offset from the source oscillation (tide) that varies spatially. Waves in plume density have a different wavelength and thus phase offset from the source. Variable-mixing cases have a spatially uniform plume velocity oscillation that is in phase with that of the ambient flow. Standing waves in density and thickness are antiphased with each other and are of spatially variable amplitude; density waves are zero amplitude at multiples of $\mathcal{A}$.

In both cases, the density perturbations carried by the plume have a wavelength of $\mathcal{A} = \overline{U}P$. Therefore, we may characterize the overall importance of the results presented in this paper to any particular plume by considering the value of the dimensionless ratio $\mathcal{P} = \overline{U}P/L$, where L is the "plume length." This is the length scale of interest to any particular scientific question, such as the modification of dense shelf waters as they travel downslope. A general choice of L would be the distance from the plume source to its termination at the foot of the slope or its neutral depth, but it could be chosen smaller than this if a particular fraction of the plume were of interest. Here, $\mathcal{P}$ can be viewed either as a ratio of length scales (advective length to plume length) or time scales (oscillation period to advective time). If $\mathcal{P} \approx 1$, a parcel of plume water travels exactly one plume length per forcing cycle, plume density contains one wave, and the amplitude of the complete waves experienced by the plume is maximal. If $\mathcal{P} \gg 1$, the entire plume oscillates slowly, rather than containing complete waves, and at each time the result approximates a single normal state within the "bracketed" range. If $\mathcal{P} \ll 1$, there are many waves in the plume, and this severely limits their amplitude. The waves are caused by the advection of a density anomaly, so wave amplitude will be limited if little advection occurs before the density anomaly is reversed.

Figure 10 shows the results of pulsed-source (D3–D5) and variable-mixing (U4, U6, and U7) simulations with periods of $P = 12$, 24, and 48 h. If we consider a plume with an arbitrarily chosen length of $L = 50$ km (the dashed line), this corresponds to $\mathcal{P} \approx 0.5$, 1, and 2, respectively. If the oscillation reverses rapidly (small $\mathcal{P}$),

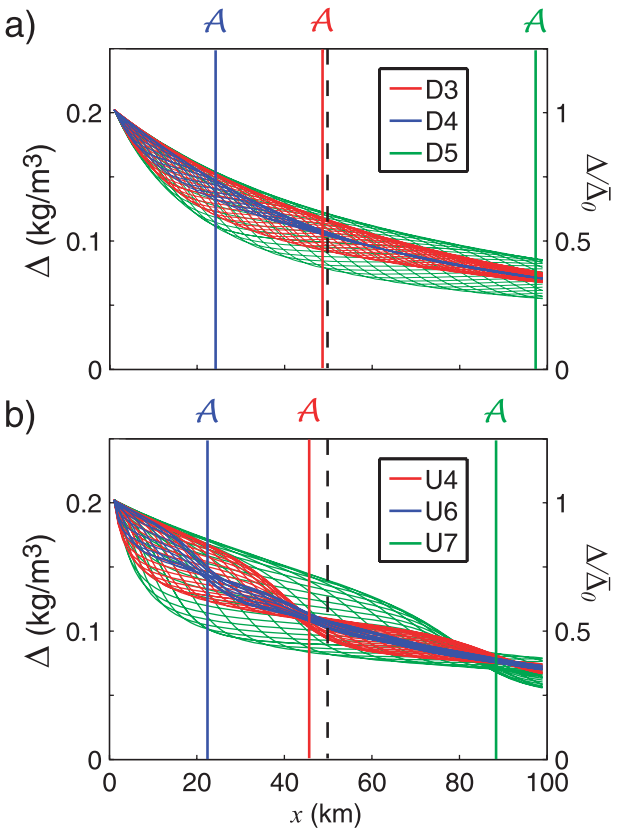

FIG. 10. Density anomaly results from the cyclic equilibria of runs (a) D3–D5, in which the source thickness oscillates with periods of 24, 12, and 48 h, respectively, and (b) U4, U6, and U7, in which the ambient flow oscillates with periods of 24, 12, and 48 h, respectively. Results are plotted every P/24 h for the final cycle P of each run. The dashed line shows $x = 50$ km as referred to in the text. If the oscillation is rapid (D4 and U6), the amplitude of the oscillations is limited, whereas, if the oscillation is slow (D5 and U7), then only part of the cycle shown affects the plume at any one time.

little advection occurs during each period of anomalous forcing and the wave amplitude is limited. If the oscillation reverses slowly (large $\mathcal{P}$), the amplitude of the anomaly is larger, but a parcel will only experience a small part of the forcing cycle before leaving the plume. Figure 10 uses a domain of length $2L$ to show the full oscillation in the $P = 48$ h ($\mathcal{P} \approx 2$) case; only half of this oscillation is experienced by a plume with $L = 50$ km.

Wavelengths are roughly constant in space because the flow velocity is relatively uniform. In the more general case of nonuniform flow, the wavelength will vary according to the local value of UP. For example, this would happen if a pulsed plume source has a slow additional variability or if a tidal flow responsible for variable mixing is not spatially uniform. Oscillation periods relative to a static observer are always fixed to the imposed P.

Variability similar to that predicted here would be challenging to observe. Resolving waves would require sampling to be spatially finer than $\mathcal{A}$ and temporally more frequent than P. Sampling over a period much greater than P would be required to average tidal effects and observe a mean plume. Such requirements are practical for ship-based sampling in a few areas but elsewhere might be met only by a mooring array. Detiding observed velocities using a barotropic model should work well for the velocities predicted in the variable-mixing simulations but cannot represent the pulsed-source waves in velocity. Waves in plume thickness and density could be impossible to remove other than by time-averaging. The observation site is important because pulsed-source cases have different wavelengths for each state variable and variable-mixing cases have standing waves whose unsteady behavior is variable in space. The different characteristics of pulsed-source and variable-mixing cases and of interfacial- and boundary-led mixing might be distinguishable from observation.

It is worth reviewing the chief limitations of the model used here. The neglect of rotation is the most obvious flaw, but the essence of these conclusions should apply to variability along the Ekman-, tide-, and topography-controlled plume path. The neglect of eddies is a fundamental problem, and baroclinic instability may obscure the variations described here. The ambient is modeled as homogeneous, but in reality a stratified ocean would permit the existence of detraining gravity currents rather than the entraining plumes modeled here and stratification would also permit internal waves or tides to radiate out into the ambient. The addition of a second horizontal dimension would introduce an additional decay in the amplitude of the waves as a result of lateral spreading. Interfacial waves could break, leading to dramatically enhanced entrainment. The tidal forcing is represented as a single harmonic and neglects the complexities of the full tidal signal, which would also be advected down the plume. We ignore the effects of mean ambient flow, such as that associated with the Antarctic Slope Front and tidal residuals. The velocity of the model plume must always be downslope and greater than that of the tide, whereas extreme cases featured in the literature have a tide that drags the plume downslope or upslope. Despite these caveats, it is hoped that the results are of some use in the interpretation of observations and formation of hypotheses.

5. Ross Sea

The model's ability to explain observations is limited, but the comparison is informative in any case. The most comprehensive studies of tidally affected dense plumes

are in the Ross Sea, Antarctica. Spring tides in this region are too extreme to be represented by the present model, but less active parts of the spring–neap cycle might be reasonably captured. The densest shelf water exits via the Drygalski Trough, increasing in thickness from 100 m at the 600-m-deep shelf break to 400 m at a 1200-m depth and 600 m farther downslope (Gordon et al. 2004, 2009; Muench et al. 2009). The mean current flows at 0.4–0.6 m s^{-1} at 35° to the isobaths, and the plume density anomaly varies up to a value of 0.2 kg m^{-3}.

Ross Sea tides are dominated by diurnal-period harmonics with a fortnightly spring–neap cycle on which the maximum tidal current varies between 0.2 and 1 m s^{-1} (Whitworth and Orsi 2006; Muench et al. 2009; P09; Wang et al. 2010). For about half of this cycle, the maximum tidal currents are larger than mean downslope flow, so tides have a profound influence on the plume. During neap tides, the shelf is permanently stratified, and a relatively steady dense plume presumably occurs (Whitworth and Orsi 2006). During spring tides, the Antarctic Slope Front is advected to the shelf break and back every tidal cycle (Whitworth and Orsi 2006; P09; Wang et al. 2010), intermittently releasing dense waters onto the slope. In both phases, tidal currents force the plume to deviate from a simple rotation- and topography-controlled path (P09).

At its mean velocity, the Drygalski Trough plume covers the distance from shelf break to its last recorded location 50 km to the northwest in approximately 1 day. The dominant tides are of diurnal period, so $\mathcal{P} \approx 1$ and the observed plume is the length of one wave in the tidally modulated quantities. Our model suggests that these are the conditions for maximum tidal effect on the plume.

Tides also play a significant role in mixing the Ross Sea plume (Muench et al. 2009; P09; Wang et al. 2010). Plume volume increases by a factor of 4 over its 50-km path, which with a transit time of ≈1 day implies an entrainment velocity of 200–400 m day^{-1} of overlying water into the plume (Gordon et al. 2009; Muench et al. 2009). The source of the turbulence responsible for this mixing is harder to ascertain. Muench et al. (2009) obtained interfacial stresses of 0.7 Pa and benthic stresses of 0.9 (neap) and 1.5 Pa (spring) and suggest that both might be significant in the plume momentum balance and downstream dilution. This stands in contrast to the nontidal case in which interfacial stress alone is usually thought to govern entrainment. If it were possible to observe the unsteady features modeled here, the different qualitative behavior offered by different entrainment parameterizations could provide insight into the dominance of boundary or interfacial mixing. In particular, in the variable-mixing cases interfacial shear is largest when the tide is directed upslope, whereas boundary mixing is largest when the tide is directed downslope.

In the Ross Sea, the benthic layer thickness varies by hundreds of meters on tidal time scales (Whitworth and Orsi 2006; Muench et al. 2009; P09). According to the model results, this would generate interfacial gravity waves with similar amplitudes, traveling at the plume velocity plus gravity wave propagation. The magnitude of entrainment waves is harder to predict because it is poorly constrained by our lack of knowledge of entrainment processes.

P09 present results from a three-dimensional baroclinic tidal model of Drygalski Trough, concentrating on spring tides. They conclude that most variability at their point 2 on the slope is associated with intermittent sampling of a plume that is laterally advected past. The difficulty in observing the behavior of this ''moving target'' partly motivates this study but complicates the comparison of the present fixed-path results to those of P09. At point 2, their bottom flow first follows the ebb tide downslope and then continues to accelerate when the dense flow appears at the turn of the tide (their Fig. 14). Peak bottom flow is at slack tide, and the current decelerates on the flood tide until the bottom flow reverses. For part of the cycle, the barotropic and benthic flows therefore have a phase offset of $P/4$. This is never consistent with variable-mixing plumes, which have a negligible phase difference between ambient and plume velocity, but does apply to pulsed-source plumes at a position close to $\mathcal{L}/4$ (Figs. 2, 3). The present study suggests that point 2 is approximately $\mathcal{L}/4$ away from point 1, which might be considered the source, so the results seem to agree with P09 that most variability in the Ross Sea plume is associated with the pulsing of its source due to advection of hydrographic gradients.

Wang et al. (2010) show an individual plume formation event at spring tide, highlighting a pulse of dense shelf water that is released onto the slope and then traverses it under the influence of rotation. The authors ascribe the thickness of this traveling pulse to vigorous tide-driven mixing, because such pulses are not modeled during neap tides. The present study suggests that the traveling pulse is governed by the intermittent source, with its thickness explained by high ''background'' tidal mixing rather than unsteady mixing during the transit of the plume. Both P09 and Wang et al. (2010) suggest that the mean plume thickness increases under more vigorous tides, implying a greater entrainment. Both the interfacial- and boundary-shear entrainment formulations tested here are nonlinear functions of plume velocity, so their entrainment will increase on average with greater tidal forcing.

Both Muench et al. (2009) and P09 perform local calculations to determine tidal effects on bottom Ekman layer thickness and transport. Their Ekman layer transport is proportional to benthic stress, which is taken as the square of the flow velocity, so the addition of tides to the mean plume velocity increases the Ekman flux considerably. The full model results of P09 agree with the calculations: stronger-tide cases have a thicker benthic boundary layer with a similar mean flow and therefore a larger depth-integrated transport. A notable qualitative result of the present study is that the effects of tides on plumes are not solely local; plume behavior at any given location is determined by advection of the accumulated history of mixing and source strength past that point.

The applicability of these results to plumes other than in the Ross Sea may be determined by considering the appropriate value of $\mathcal{P}$. For example, tidal effects are much less relevant to the plume of dense shelf water that flows down the Filchner Depression in the Weddell Sea, Antarctica, because $\mathcal{P} \approx 0.2$ there ($\overline{U} \approx 0.2$ m s^{-1}, $P \approx$ 24 h, and $L \approx 100$ km; Foldvik et al. 2004). However, variability with periods of up to 6 days ($\mathcal{P} \approx 1.2$) is also observed in that region (Darelius et al. 2009), and this longer-period variability might have a similar total impact on the Filchner Depression as the diurnal tide has on the Drygalski Trough.

6. Summary

The descent of dense-water plumes down continental slopes is an important component of the global ocean circulation that is commonly affected by tidal influence on the plume source, mixing, and path. In this study, a simple one-dimensional model is used to isolate the first two effects. Oscillating forcings are advected by the plume, creating traveling gravity waves in the case of a pulsed source and standing entrainment waves in the case of time-variable mixing. The two different effects might be distinguishable from observation. Wavelengths are determined by advective and gravity wave propagation length scales, and amplitudes are determined by considering the normal state of plumes with steady forcings corresponding to the extreme values of the oscillating cases. The effects of the waves illustrated here are most important when the advective length scale is equal to the plume length: that is, when $\mathcal{P} = \overline{U}P/L \approx 1$.

A practical example of these effects is of dense water cascading off the Ross Sea continental shelf. Observations suggest that $\mathcal{P} \approx 1$ for the strong diurnal tides in the region, implying that conditions are conducive to the behavior described here. Modeled effects of a pulsing source are qualitatively in agreement with observations, whereas those of time-variable mixing are not. The present study therefore agrees with earlier conclusions that hydrographic variability on the slope is associated with variability in the supply of dense water at the shelf break, rather than variation in plume mixing.

The practical utility of the results from this simple model is limited by the stringent assumptions made in its formulation. The goal here is to evaluate and distinguish some of the tidal variability that might occur along the meandering plume path. The model is complementary to more detailed approaches, because its simplicity reveals some underlying concepts, such as the ''nonlocality'' of plume properties; the hydrography observed at a point on the plume is determined by the time history of tidal effects, which are integrated by plume advection. When this variability is added to the tidal excursion of the plume path, there is considerable scope for aliasing of plume properties in the observations from a typical oceanographic section.

Acknowledgments. This paper has benefited considerably from insightful comments made by Adrian Jenkins and five anonymous reviewers.

APPENDIX

''Normal State'' Velocity Boundary Conditions

Steady plumes adjust from arbitrary source conditions to a steady normal-state velocity, which in the ET59 case is determined by a balance between buoyancy and drag. This adjustment is rapid; the unsteady term in (12) is smaller than the buoyancy term after $U^*x^*/g'^*I^* \approx 7$ h using scales of $U^* = 0.5$ m s^{-1}, $g'^* = 2 \times 10^{-3}$ m s^{-2}, and $I^*/x^* = 10^{-2}$. In this study, we are interested in oscillations in the normal state rather than the adjustment, so we wish to set the source flow velocity to the oscillating normal state. Previous authors have obtained a quadratic expression for the normal velocity by assuming a force balance in the momentum equation (e.g., Mahrt 1982), so that theory is extended here to the unsteady case.

Seeking $\partial U/\partial x = 0$ and using the entrainment formulation (19) under the assumption that $U \geq U_a$, (2) and (12) become

$$\frac{\partial D}{\partial t} + U\frac{\partial D}{\partial x} = E(U - U_a) \quad \text{and} \tag{A1}$$

$$\frac{\partial (DU)}{\partial t} + U^2\frac{\partial D}{\partial x} = g'D\left(\frac{\partial B}{\partial x} - \frac{\partial D}{\partial x}\right) + D\frac{\partial U_a}{\partial t} + E(U - U_a)U_a - cU^2. \tag{A2}$$

If we now assert that $\partial D/\partial t = 0$ at the inflow (see below), (A1) becomes

$$\frac{\partial D}{\partial x} = E\frac{(U - U_a)}{U}, \tag{A3}$$

so (A2) becomes

$$D\frac{\partial U}{\partial t} = -(E + c)U^2 + 2EU_aU + \left(g'D\frac{\partial B}{\partial x} - g'DE + D\frac{\partial U_a}{\partial t} - EU_a^2\right) + \frac{g'DEU_a}{U}. \tag{A4}$$

This equation underlies the momentum source condition used in all cases. Note that the entrainment formulation is integral to the derivation, so (A4) must be rederived if other parameterizations are used. The simpler simulations use a reduced form of (A4), as detailed in Table 1, so we now consider each case individually.

a. Steady source with stagnant or steadily flowing ambient

When there is no flow in the ambient or unsteady behavior in the plume, (A4) reduces to the quadratic equation obtained by many previous authors (e.g., Mahrt 1982). This has one positive real root, which is used as the source plume velocity. In the steady state of a plume forced by steady ambient flow, (A4) becomes a cubic equation. Analysis of the discriminant and roots of this equation shows that for all reasonable cases there are three real roots of which only one is positive, so this is used as the source plume velocity. These plumes are initiated in their steady normal states.

b. Steady source with unsteady ambient flow

In the fully unsteady variable-mixing cases, the full ordinary differential equation (A4) is integrated. The integral converges to steady state before the oscillating ambient is activated (see section 2f), and subsequent evolution is obtained by integrating forward from that state. These plumes are sourced in their instantaneous normal state at each stage of the unsteady forcing.

c. Unsteady source with stagnant ambient

Pulsed-source simulations are driven by unsteady-source properties, which are translated into spatial gradients as the plumes advect properties downstream. It is therefore impossible for the standard normal state with $D \sim x$ and $\Delta \sim x^{-1}$ to exist at the source. Instead, we seek those conditions that most closely match $\partial U/\partial x = 0$. Experimentation with the available choices shows that using the quadratic expression described above fulfills this requirement. This amounts to asserting that the plume source instantaneously achieves force balance between buoyant acceleration and turbulent drag as its properties are varied.

REFERENCES

Baba, N., K. Kitaura, Y. Sakaguchi, and K. Kuwajima, 2000: Gravity current in an oscillatory flow (in Japanese). *J. Kansai Soc. Nav. Archit. Japan,* **187,** 193–199.

——, ——, ——, ——, and K. Arai, 2001: Experiment on the behaviour of the head of gravity current in an oscillatory flow (in Japanese). *J. Kansai Soc. Nav. Archit. Japan,* **235,** 213–218.

Baines, P. G., 2005: Mixing regimes for the flow of dense fluid down slopes into stratified environments. *J. Fluid Mech.,* **538,** 245–267, doi:10.1017/S0022112005005434.

——, 2008: Mixing in downslope flows in the ocean—Plumes versus gravity currents. *Atmos.–Ocean,* **46,** 405–419, doi:10.3137/ao.460402.

——, and S. Condie, 1998: Observations and modelling of Antarctic downslope flows: A review. *Ocean, Ice, and Atmosphere: Interactions at the Antarctic Continental Margin,* S. S. Jacobs and R. F. Weiss, Eds., Antarctic Research Series, Vol. 75, Amer. Geophys. Union, 29–49.

Cenedese, C., and C. Adduce, 2010: A new parameterization for entrainment in overflows. *J. Phys. Oceanogr.,* **40,** 1835–1850.

Choutapalli, I., A. Krothapalli, and J. H. Arakeri, 2009: An experimental study of an axisymmetric turbulent pulsed air jet. *J. Fluid Mech.,* **631,** 23–63.

Darelius, E., L. H. Smedsrud, S. Østerhus, A. Foldvik, and T. Gammelsrød, 2009: Structure and variability of the Filchner overflow plume. *Tellus,* **61A,** 446–464, doi:10.1111/j.1600-0870.2009.00391.x.

Ellison, T. H., and J. S. Turner, 1959: Turbulent entrainment in stratified flows. *J. Fluid Mech.,* **6,** 423–448.

Erofeeva, S. Y., L. Padman, and G. Egbert, 2005: Assimilation of ship-mounted ADCP data for barotropic tides: Application to the Ross Sea. *J. Atmos. Oceanic Technol.,* **22,** 721–734.

Foldvik, A., and Coauthors, 2004: Ice shelf water overflow and bottom water formation in the southern Weddell Sea. *J. Geophys. Res.,* **109,** C02015, doi:10.1029/2003JC002008.

Gordon, A. L., E. Zambianchi, A. Orsi, M. Visbeck, C. F. Giulivi, T. Whitworth III, and G. Spezie, 2004: Energetic plumes over the western Ross Sea continental slope. *Geophys. Res. Lett.,* **31,** L21302, doi:10.1029/2004GL020785.

——, A. H. Orsi, R. Muench, B. A. Huber, E. Zambianchi, and M. Visbeck, 2009: Western Ross Sea continental slope gravity currents. *Deep-Sea Res. II,* **56,** 796–817, doi:10.1016/j.dsr2.2008.10.037.

Hansen, B., and S. Østerhus, 2000: North Atlantic–Nordic Seas exchanges. *Prog. Oceanogr.,* **45,** 109–208.

Hogg, A. J., and D. Pritchard, 2004: The effects of hydraulic resistance on dam-break and other shallow inertial flows. *J. Fluid Mech.,* **501,** 179–212, doi:10.1017/S0022112003007468.

——, M. A. Hallworth, and H. E. Huppert, 2005: On gravity currents driven by constant fluxes of saline and particle-laden fluid in the presence of a uniform flow. *J. Fluid Mech.,* **539,** 349–385, doi:10.1017/S002211200500546X.

Ivanov, V. V., G. I. Shapiro, J. M. Huthnance, D. L. Aleynik, and P. N. Golovin, 2004: Cascades of dense water around the World Ocean. *Prog. Oceanogr.,* **60,** 47–98, doi:10.1016/j.pocean.2003.12.002.

Jacobs, S. S., 1991: On the nature and significance of the Antarctic Slope Front. *Mar. Chem.,* **35,** 9–24.

Killworth, P. D., and N. R. Edwards, 1999: A turbulent bottom boundary layer code for use in numerical ocean models. *J. Phys. Oceanogr.,* **29,** 1221–1238.

Legg, S., R. W. Hallberg, and J. B. Girton, 2006: Comparison of entrainment in overflows simulated by z-coordinate, isopycnal, and non-hydrostatic models. *Ocean Modell.,* **11,** 69–97, doi:10.1016/j.ocemod.2004.11.006.

Lighthill, M. J., 1978: *Waves in Fluids*. Cambridge University Press, 504 pp.

Mahrt, L., 1982: Momentum balance of gravity flows. *J. Atmos. Sci.,* **39,** 2701–2711.

Muench, R. D., L. Padman, A. Gordon, and A. Orsi, 2009: A dense water outflow from the Ross Sea, Antarctica: Mixing and the contribution of tides. *J. Mar. Syst.,* **77,** 369–387, doi:10.1016/j.jmarsys.2008.11.003.

Osborn, T. R., 1980: Estimates of the local rate of vertical diffusion from dissipation measurements. *J. Phys. Oceanogr.,* **10,** 83–89.

Padman, L., and S. Erofeeva, 2004: A barotropic inverse tidal model for the Arctic Ocean. *Geophys. Res. Lett.,* **31,** L02303, doi:10.1029/2003GL019003.

——, S. L. Howard, A. H. Orsi, and R. D. Muench, 2009: Tides of the northwestern Ross Sea and their impact on dense outflows of Antarctic Bottom Water. *Deep-Sea Res. II,* **56,** 818–834, doi:10.1016/j.dsr2.2008.10.026.

Price, J. F., and M. O. Baringer, 1994: Outflows and deep water production by marginal seas. *Prog. Oceanogr.,* **33,** 161–200.

Scase, M. M., C. P. Caulfield, S. B. Dalziel, and J. C. R. Hunt, 2006: Time-dependent plumes and jets with decreasing source strengths. *J. Fluid Mech.,* **563,** 443–461, doi:10.1017/S0022112006001212.

——, A. J. Aspden, and C. P. Caulfield, 2009: The effect of sudden source buoyancy flux increases on turbulent plumes. *J. Fluid Mech.,* **635,** 137–169, doi:10.1017/S002211200900740X.

Simpson, J. E., and R. E. Britter, 1980: A laboratory model of an atmospheric mesofront. *Quart. J. Roy. Meteor. Soc.,* **106,** 485–500.

Smith, P. C., 1975: A streamtube model for bottom boundary currents in the ocean. *Deep-Sea Res.,* **22,** 853–873.

Turner, J. S., 1986: Turbulent entrainment: The development of the entrainment assumption, and its application to geophysical flows. *J. Fluid Mech.,* **173,** 431–471.

Wang, Q., S. Danilov, H. H. Hellmer, and J. Schröter, 2010: Overflow dynamics and bottom water formation in the western Ross Sea: Influence of tides. *J. Geophys. Res.,* **115,** C10054, doi:10.1029/2010JC006189.

Whitham, G. B., 1974: *Linear and Nonlinear Waves*. Wiley, 636 pp.

Whitworth, T., III, and A. H. Orsi, 2006: Antarctic Bottom Water production and export by tides in the Ross Sea. *Geophys. Res. Lett.,* **33,** L12609, doi:10.1029/2006GL026357.